*Structural Analysis of Historical Constructions – Jerzy Jasieńko (ed)*
*© 2012 DWE, Wrocław, Poland, ISSN 0860-2395, ISBN 978-83-7125-216-7*

# FINITE ELEMENT SIMULATIONS FOR THE COMPREHENSION OF PHYSICAL PHENOMENA INVOLVED IN ELECTRIC IMPEDANCE TOMOGRAPHY OF MASONRY STRUCTURES

*Alcantara Naasson*[1], *Ramos Luís F.*[2], *Mendes Paulo*[3], *Ferreira João*[4], *Fernandes Francisco*[5], *Lourenço Paulo B.*[6]

## ABSTRACT

The paper describes the preliminary studies of University of Minho on the use of Electric Impedance/Resistance Tomography to assess masonry structures. The study is focused on the analysis of values of current and voltage resulting from the use of an electrical source with voltage and frequency values from a distribution network. The analysis is made from results obtained through computer simulations, using a three-dimensional model of the idealized masonry structures. A finite element program was used for the simulations. Three types of electrodes were used in simulations, and the analysis of the results led to significant conclusions. Later masonry specimens were built and a series of preliminary tests were carried out in the laboratory. The comparative analysis of simulated and experimental results allowed identifying the factors that have influence on the physical results.

*Keywords:* *Non-Destructive Test, Electrical Impedance/Resistance Tomography, Masonry Structures*

## 1. INTRODUCTION

Electrical Resistance/Impedance Tomography (ERT/EIT) belongs to the group of Non-Destructive electric methods aiming at obtaining a 3D image of the inner parts of a structure through measurements of its electrical properties [1]. A picture of the electrical conductivity distribution inside an investigated object is produced on the basis of measurements of electric potential distribution on its surface. The distribution of conductivity is determined through repeated measurements (for different configurations of the excitation probes) of potentials on the surface of the structure. The main difficulty in this method consists in experimentally determining the dependence between conductivity distribution and the anomalies within the investigated structure. The distribution of electric potentials on the surface of an object depends on the distribution of conductivity inside the object. Surface potential measurements are performed at different projection

[1] Associate Professor – PhD, Electrical Engineering Department, São Paulo State University, Bauru/SP, Brazil, naasson@feb.unesp.br
[2] Assistant Professor – PhD, ISISE, Civil Engineering Department, University of Minho, Guimarães, Portugal, lramos@civil.uminho.pt
[3] Assistant Professor – PhD, ALGORITMI, Electronic Engineering Department, University of Minho, Guimarães, Portugal, Paulo.mendes@dei.uminho.pt
[4] Research Assistant – MSc, ISISE, Civil Engineering Department, University of Minho, Guimarães, Portugal, j.f.ferreira@hotmail.com
[5] Assistant Professor – PhD, ISISE, Lusíada University, Vila Nova de Famalicão, Portugal, francisco.fernandes@fam.ulusiada.pt
[6] Full Professor – PhD, ISISE, Civil Engineering Department, University of Minho, Guimarães, Portugal, pbl@civil.uminho.pt

angles whereby enough information is acquired to determine the distribution of conductivity inside the structure.
Electrical Resistance Tomography has been used in geophysics inspections for many decades, with a reasonable degree of success [2-4]. In the last few years some researchers have tried to use it as an alternative technique for masonry inspections [5-7]. Differing to the situation for soil investigation in geophysics, the limited dimensions of masonry structures and the high degree of heterogeneity (complexity) complicates the interpretation of the measurements.
The objective of this paper is to analyze the behavior of different electric variables in an ERT, as a function of the type of electrodes and the dimensions of the possible anomalies present inside the masonry structures. This analysis will be based on finite element simulations and on a preliminary experimental campaign. The final goal of this work is to improve the ERT with the aim of identifying damages in historical masonry constructions. Therefore, the paper is organized by following: Section 1 gives the introduction; Section 2 presents the problem to be addressed in this work by means of four masonry specimens built in the laboratory for testing the Electric Impedance Tomography; Section 3 presents the numerical simulation considering different positions for the electrodes, as well as their size and shape; Section 4 discuss the results of the numerical; Section 5 compares the numerical results with the first experimental trials; and Section 6 presents the conclusions.

## 2. THE PROPOSED PROBLEM

The problem proposed in this paper is to characterize the expected voltage and currents in small masonry specimens when a low-frequency electrical voltage is applied on their surfaces. Four masonry specimens with 570 × 420 × 340 mm$^3$ were constructed for this purpose. Each specimen was built using 36 ceramic bricks with 220 × 110 × 60 mm$^3$, creating a two leave masonry wall with an inner leaf with 120 mm of thickness, according to the illustration in Fig. 1. Lime based mortar was used in all specimens.

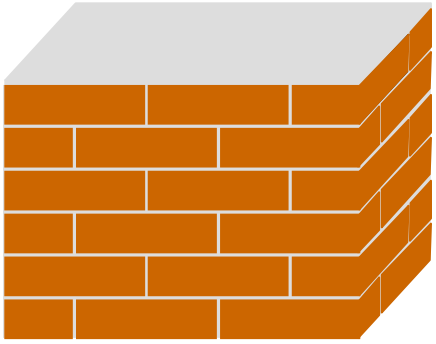

**Fig. 1** Masonry specimens used for the analysis (570 × 420 × 340 mm$^3$)

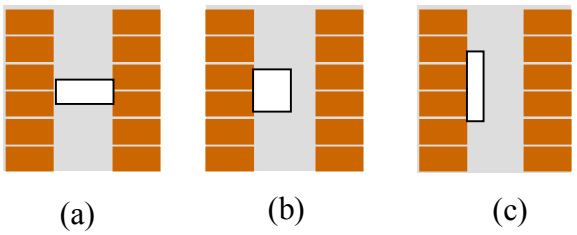


**Fig. 2** Voids inserted in the specimens. (a) Void 1 with 160 × 160 × 40 mm$^3$; (b) Void 2 with 120 × 70 × 80 mm$^3$; and (c) Void 3 with 90 × 40 × 120 mm$^3$

The first specimen was considered without any damage (void) inside. The inner space between the leaves for this reference specimen was fully filled with mortar. On the other specimens, a damage scenario was simulated by inserting a void by means of Styrofoam block, as shown in Fig. 2. As stressed before, the purpose of the work is to analyze how the voltage and current behaves cording to the size and shape of the electrodes, and to correlate the measurements with the "voids" inserted in the specimens. To facilitate the writing and reading of the text, the specimens will be identified by the following abbreviations: BR – specimen without any void; $BD_1$ – specimen with the Void 1; $BD_2$ – specimen with the Void 2 and $BD_3$ – specimen with the Void 3.

## 3. NUMERICAL SIMULATIONS

The simulations were carried out using the finite element program Ansys®. Tetrahedron elements were used, resulting four models with about 300,000 elements and 500,000 nodes.
Three kinds of electrodes were used in the simulations: (a) a long-pin electrode (LPE), with 5 mm diameter and 60 mm of insertion within the joint; (b) a short-pin electrode (SPE), with 8 mm diameter

and 30 mm of insertion within the mortar; (c) and a slab type electrode (STE), with cross area of 20 × 10 mm$^2$ and 10 mm of insertion within the joint.
Eighteen electrodes were placed on two parallel surfaces of the specimen, configuring nine electrode positions, according illustration in Fig. 3. In each simulation, a 100 $V_{rms}$ with 50-Hz electric voltage was applied between the electrodes of a given position, and the value of the electrical current between these electrodes, as well as the values of the voltage between the other electrodes, was calculated.

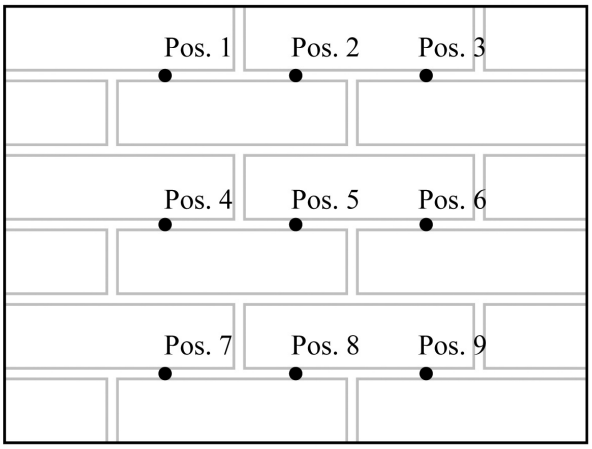


**Fig. 3** Illustration of the electrode positions on the masonry specimen

## 4. RESULTS OF THE SIMULATIONS

Fig. 4 shows the voltage distribution when the voltage is applied at positions 1 (left side), and 5 (right side), for the BR specimen and LPE electrode.

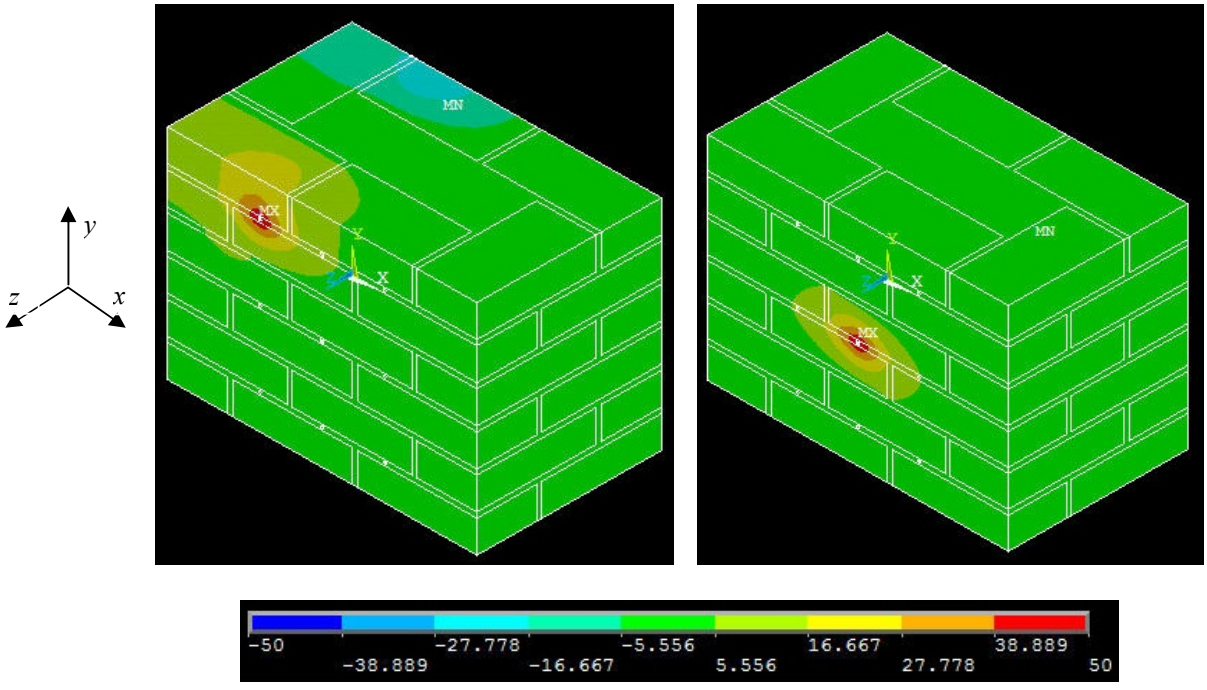


**Fig. 4** Voltage distribution on the surface of the specimen: left side – input voltage applied between the electrodes of the position 1; right side – input voltage applied between the electrodes of the position 5

Figures 5 to 7 show the current distribution in a plane located at $z$ = 170 mm, for specimens BR, $BD_1$, $BD_2$ and $BD_3$, respectively, when the LPE, SPE and STE electrodes are used.
For Figures 5a, 6a and 7a (BR specimen), the current distribution is concentrated at the center of the specimen. The highest value of the current density, represented by the red color, occurs between 0.242 and 0.272 A/m$^2$ for the LPE electrode, 0.147 and 0.166 A/m$^2$ for the SPE electrode, and 0.113 and 0.127 A/m$^2$ for the STE electrode.

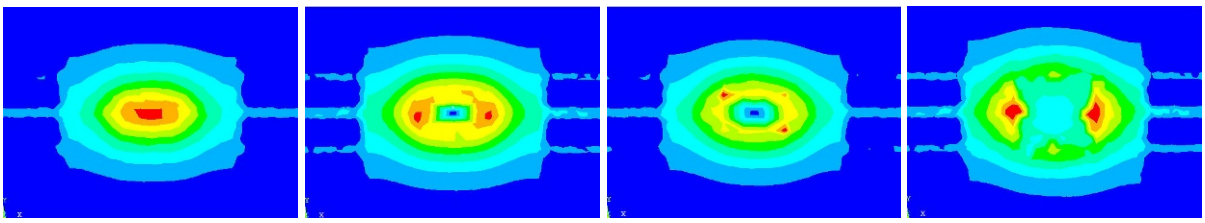

(a) (b) (c) (d)

**Fig. 5** Current distribution at plane $z$ = 170 mm, excitation at Position 5, LPE electrode: (a) BR specimen; (b) $BD_1$ specimen; (c) $BD_2$ specimen; (d) $BD_3$ specimen

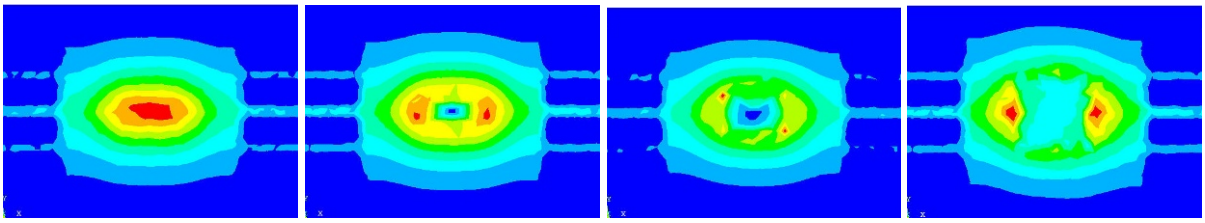

(a) (b) (c) (d)

**Fig. 6** Current distribution at plane $z$ = 170 mm, excitation at Position 5, SPE electrode: (a) BR specimen; (b) $BD_1$ specimen; (c) $BD_2$ specimen; (d) $BD_3$ specimen

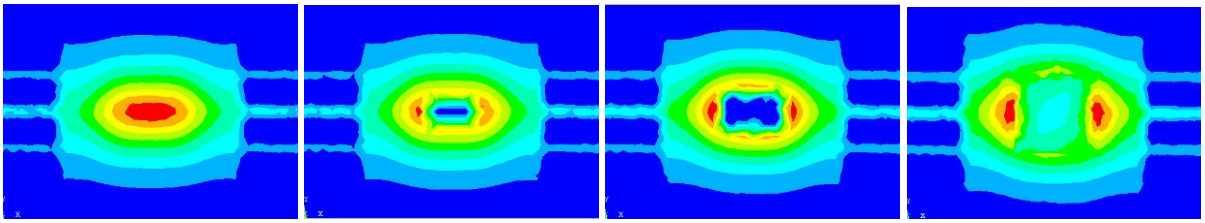

(a) (b) (c) (d)

**Fig. 7** Current distribution at plane $z$ = 170 mm, excitation at Position 5, STE electrode: (a) BR specimen; (b) $BD_1$ specimen; (c) $BD_2$ specimen; (d) $BD_3$ specimen

For figures 5b, 6b and 7b ($BD_1$ specimen), the region with high densities is divided in two regions on both lateral sides of the void. The reference plane cuts the void, and its presence is clearly defined in the pictures. The highest values of current density lie between 0.196 and 0.221 A/m$^2$ for the LPE electrode, 0.119 and 0.136 A/m$^2$ for the SPE electrode, and 0.116 and 0.130 A/m$^2$ for the STE electrode. Figures 5c, 6c and 7c ($BD_2$ specimen) present more significant differences among themselves. In Fig. 7c the void is more clearly defined than in figures 5c and 6b. The highest value of current density lie between 0.254 and 0.296 A/m$^2$ for the LPE electrode, 0.178 and 0.200 A/m$^2$ for the SPE electrode, and 0.112 and 0.125 A/m$^2$ for the STE electrode. In these cases, the reference plane also cut the void. Finally, for figures 5d, 6d and 7d the regions with highest current densities were split in two other regions on both sides of the void. In these cases, the reference plane doesn't cut the void, but its presence is still defined in the current density maps. The highest values of current density lie between 0.216 and 0.243 A/m$^2$ for the LPE electrode, 0.153 and 0.172 A/m$^2$ for the SPE electrode, and 0.110 and 0.125 A/m$^2$ for the STE electrode.

As new illustration for the current distribution, figures 8 to 10 present the density maps when the voltage excitation is applied between the electrodes at the Position 2.

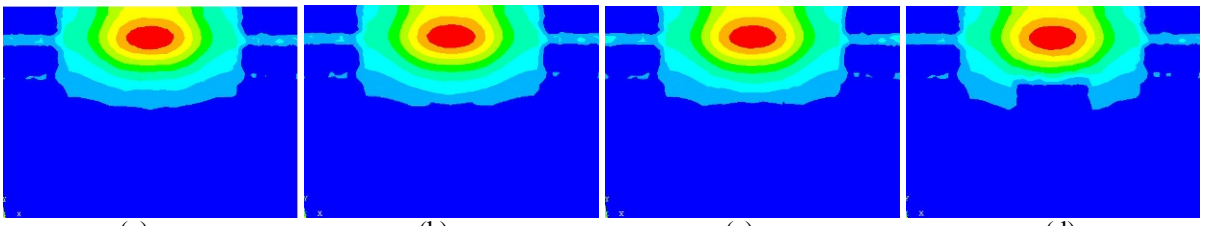

(a) (b) (c) (d)

**Fig. 8** Current distribution at plane $z$ = 170 mm, excitation at Position 2, LPE electrode: (a) BR specimen; (b) $BD_1$ specimen; (c) $BD_2$ specimen; and (d) $BD_3$ specimen

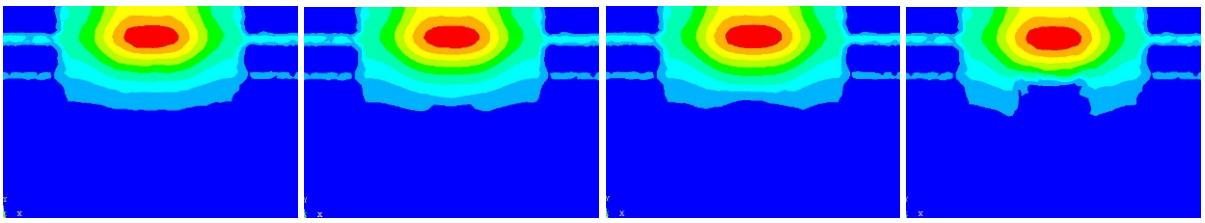

(a) (b) (c) (d)

**Fig. 9** Current distribution at plane $z$ = 170 mm, excitation at Position 2, SPE electrode: (a) BR specimen; (b) $BD_1$ specimen; (c) $BD_2$ specimen; and (d) $BD_3$ specimen

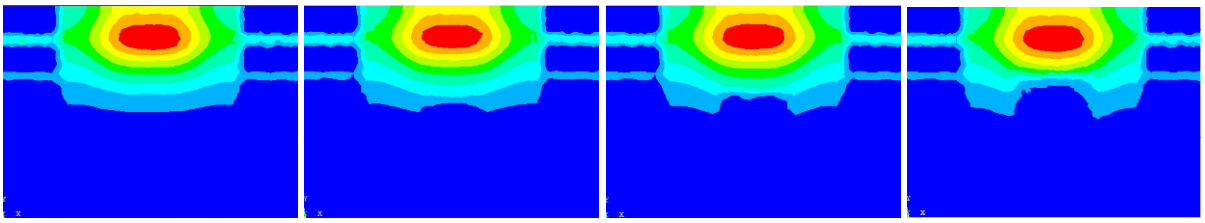

(a) (b) (c) (d)

**Fig. 10** Current distribution at plane $z$ = 170 mm, excitation at Position 2, STE electrode: (a) BR specimen; (b) $BD_1$ specimen; (c) $BD_2$ specimen; and (d) $BD_3$ specimen

Table 1 shows current results obtained at positions 1, 2, 4 and 5, for BR, $BD_1$, $BD_2$ and $BD_3$ specimens, using the LPE, SPE and STE electrodes.

**Table 1** Current (mA) for each position, electrode type and specimen

| Specimen | Position 1 | | | Position 2 | | | Position 4 | | | Position 5 | | |
|---|---|---|---|---|---|---|---|---|---|---|---|---|
| | LPE | SPE | STE | LPE | SPE | STE | LPE | SPE | STE | LPE | SPE | STE |
| **BR** | 9.20 | 6.60 | 5.40 | 9.16 | 6.53 | 5.32 | 9.58 | 6.80 | 5.56 | 9.52 | 6.74 | 5.47 |
| **$BD_1$** | 9.26 | 6.62 | 5.40 | 9.21 | 6.57 | 5.33 | 9.74 | 6.93 | 5.59 | 9.51 | 6.82 | 5.48 |
| **$BD_2$** | 9.39 | 6.63 | 5.40 | 9.33 | 6.59 | 5.33 | 10.17 | 6.71 | 5.47 | 10.42 | 7.12 | 5.59 |
| **$BD_3$** | 9.40 | 6.74 | 5.52 | 9.37 | 6.70 | 5.46 | 10.21 | 7.27 | 5.98 | 10.50 | 7.53 | 6.17 |

Fig. 11 shows the values of the current for the LPE, SPE and STE electrodes, in a graphic way. In each graph, the red line is the current for the Position 1, the green line is the current for the Position 2, the blue line is the current for the Position 4 and the black line is the current for the Position 5.

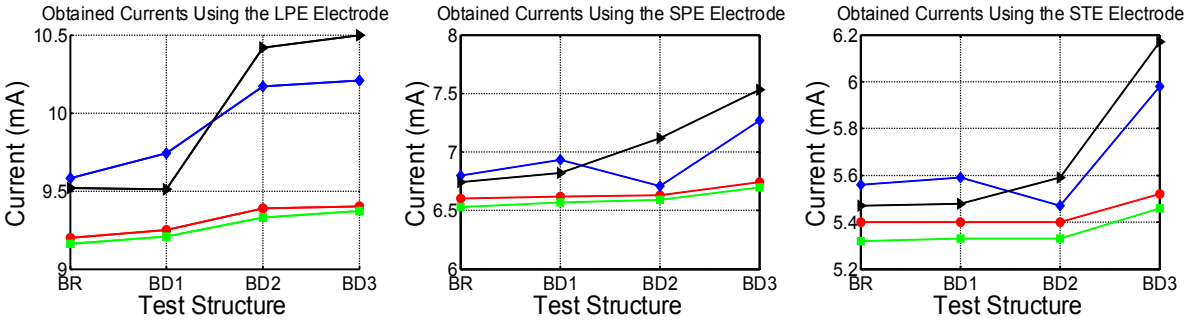


**Fig. 11** Obtained currents: (a) LPE electrode; (b) SPE electrode; and (c) STE electrode

According to these results, the values obtained at positions 1 and 2 vary slightly in function of the size of the voids, while for the measurements carried out at positions 3 and 4 these variations are more pronounced. The curves keep their patterns when changing from one type of electrode to another, but with changes on the magnitude of the current. The LPE electrode produces the highest values for the electric current.

Fig. 12 shows the relative variations of the current between adjacent electrodes. For example, in Fig. 12a, *(Pos1/Pos2)* is the relative variation calculated for the positions 1 and 2, according to:

$$(Pos1/Pos2) = 100 \times \frac{Current_{pos1} - Current_{pos2}}{Current_{pos1}} \quad (1)$$

The other points are calculated in a similar way. Each graph represents one type of electrode. In each graphic, the red line contains the values for the specimen BR, the green line contains the values for the specimen $BD_1$, the blue line contains the values for the specimen $BD_2$ and the black line contains the values for the specimen $BD_3$.

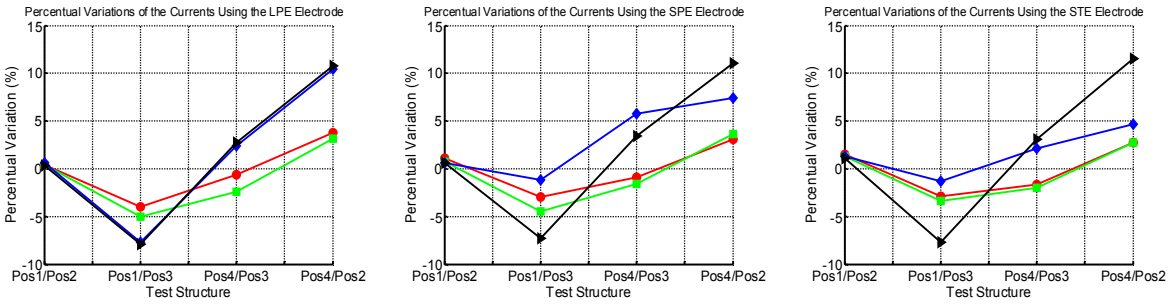


(a) (b) (c)

**Fig. 12** Relative variation of the current: (a) LPE electrode; (b) SPE electrode; and (c) STE electrode

Analyzing Fig. 12 it can be observed that the patterns of variations are also very consistent regarding the used type of electrode. However, for the LPE electrode (Fig. 12a), the curves for the $BD_2$ and $BD_3$ specimens are almost coincident, while for the specimens $BD_1$ and BR the curves are very different from each other. By the other hand, for the STE electrode (Fig. 12c) the curves for the BR and $BD_1$ specimens are almost coincident, and the curves for the specimens $BD_2$ and $BD_3$ are very different from each other. The graph in Fig. 12b (SPE electrode), shows a solution where each configuration has a well-defined curve.

Table 2 shows the voltage values at the nine pairs of electrodes, when the voltage of 100 $V_{rms}$ is applied between the central electrodes (Position 5).

**Table 2** Voltage (V) at the nine electrode positions for each type of electrode and test specimen

| Pos | BR | | | BD1 | | | BD2 | | | BD3 | | |
|---|---|---|---|---|---|---|---|---|---|---|---|---|
| | LPE | SPE | STE | LPE | SPE | STE | LPE | SPE | STE | LPE | SPE | STE |
| **1** | 0.78 | 0.67 | 0.58 | 0.82 | 0.70 | 0.61 | 0.85 | 0.73 | 0.63 | 1.03 | 0.86 | 0.74 |
| **2** | 0.90 | 0.77 | 0.67 | 0.95 | 0.81 | 0.70 | 0.99 | 0.84 | 0.73 | 1.24 | 1.07 | 0.88 |
| **3** | 0.78 | 0.67 | 0.58 | 0.81 | 0.70 | 0.61 | 0.84 | 0.72 | 0.63 | 1.04 | 0.87 | 0.75 |
| **4** | 13.48 | 12.11 | 10.83 | 13.84 | 12.43 | 10.95 | 13.99 | 12.57 | 11.22 | 16.20 | 13.28 | 11.82 |
| **5** | 100.0 | 100.0 | 100.0 | 100.0 | 100.0 | 100.0 | 100.0 | 100.0 | 100.0 | 100.0 | 100.0 | 100.0 |
| **6** | 13.40 | 12.10 | 10.83 | 13.83 | 12.41 | 11.12 | 13.98 | 12.55 | 11.23 | 16.40 | 13.28 | 11.82 |
| **7** | 0.78 | 0.67 | 0.58 | 0.82 | 0.70 | 0.61 | 0.84 | 0.72 | 0.63 | 1.04 | 0.87 | 0.75 |
| **8** | 0.90 | 0.77 | 0.67 | 0.95 | 0.81 | 0.70 | 0.99 | 0.84 | 0.73 | 1.23 | 1.03 | 0.88 |
| **9** | 0.78 | 0.67 | 0.58 | 0.81 | 0.70 | 0.61 | 0.85 | 0.73 | 0.63 | 1.03 | 0.86 | 0.74 |

In absolute terms, the voltage is less than 1 V (reduction by a factor greater than 100) in the pairs of electrodes, 1, 2, 3, 7, 8 and 9 with few exceptions. On the other hand, the voltage is greater than 10 V (reduction by a factor of 10 less) in 4 and 6 pairs of electrodes. In other words, a Voltage is greater on the electrodes placed on the same layer of the excitation electrode. For similar positions, the values obtained for the electrode LPE are slightly larger the values obtained for the SPE electrode, in turn are slightly larger the values obtained for the STE electrode.

Fig. 13 shows the attenuation with respect to 100 V for each type of electrode, calculated according the formula:

$$Attenuation_{(dB)} = 10 log\left(V_{pos.N} / 100\right) \quad (2)$$

where $V_{pos.N}$ is the voltage measured at position N. All graphs display the same pattern for the attenuations, regarding the type of electrode used.

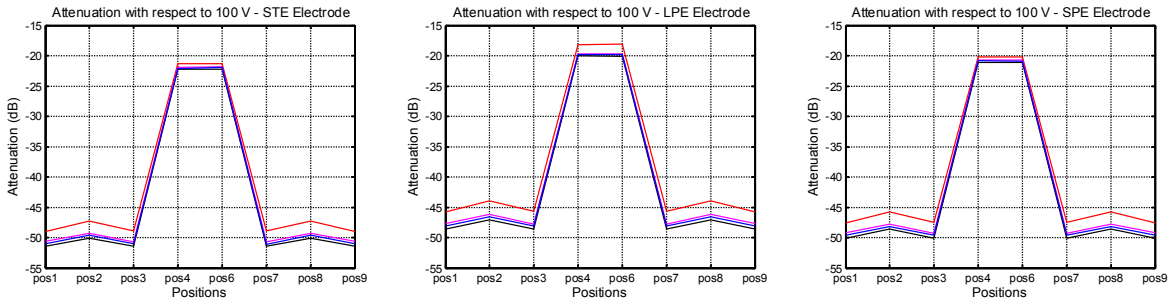


**Fig. 13** Attenuation with respect to 100 V (Black – BR specimen; blue – $BD_1$ specimen; magenta – $BD_2$ specimen; red – $BD_3$ specimen): (a) STE electrode; (b) LPE electrode; and (c) SPE electrode

Fig. 14 shows the attenuation of the voltage values obtained for specimens $BD_1$, $BD_2$ and $BD_3$ with respect to the voltage values for the BR specimen, according the formula:

$$Gain_{(dB)} = 10\log\left(V_{ET(pos.N)} / V_{BR(pos.N)}\right) \tag{3}$$

where ET stand for electrode type (LPE, SPE our STE), and (pos.N) stands for the position of the electrodes. It is easy to observe that the curves are stratified by specimens. The circular marks identify the curves for the $BD_1$ specimen, the diamond marks identify the curves for the $BD_2$ specimen and square marks identify the curves for the specimen $BD_3$. These curves show that it is possible a good discrimination between the patterns obtained for each specimen, regardless of the used type of electrode.

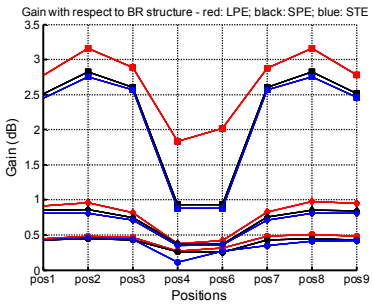


**Fig. 14** Gain with respect to similar positions in the BR specimen

## 5. COMPARISON WITH EXPERIMENTAL RESULTS

The four specimens were constructed in the Laboratory of Non-Destructive Testing of the University of Minho, as illustrated in Fig. 15, and a low cost measurement system was developed to perform the tests, as illustrated in Fig. 16. This system consists of two highly accurate digital multimeters to measure voltages and currents, one AC voltage source to apply voltage between the electrodes and one computer to record the measured values. A connection box with 24 output channels was built in the laboratory, in order to correctly select the current-injection terminals and the electrodes for the voltage measurements. The electrodes used in the real specimens were the LPE type, with 5 mm diameter and 60 mm of insertion into the mortar.

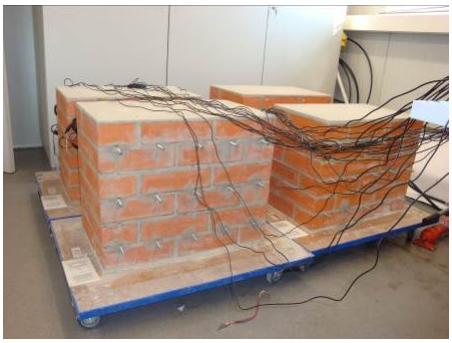

**Fig. 15** Masonry specimens for testing

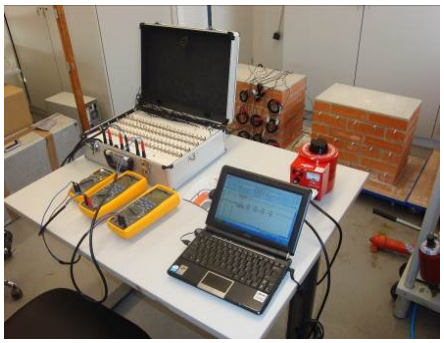

**Fig. 16** The developed measurement system

Fig. 17 shows the comparison between simulated and experimental results for the current at positions 4, 5 and 6 of each specimen. In each position, the first bar (blue) is the simulated results, the second bar (green) presents the results obtained at laboratory tests performed on 20/01/2012 (after 28 days of curing) and the third bar (brown) represents the results obtained at laboratory tests performed on 20/02/2012 (after 56 days of curing).

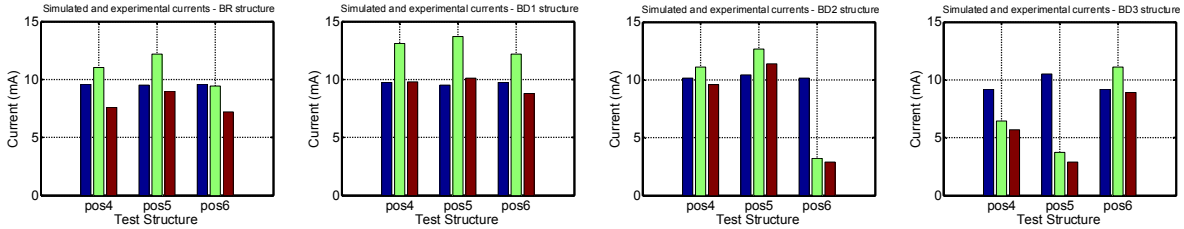


**Fig. 17** Electrical current obtained in laboratory tests (green and brown bars are the experimental results and blue bars are the numerical simulations): (a) BR specimen; (b) $BD_1$ specimen; (c) $BD_2$ specimen; and (d) $BD_3$ specimen

As we can see, the experimental results are very different from those obtained by numerical simulations. This is no surprise, because in the numerical simulations, the conductivity of the materials was considered to be homogeneous. Moreover, the materials were considered to be continuous. Of course this does not happen in a realistic situation. There is a wide variation in the values of the conductivity, due to the non-homogeneous distribution of the various elements in the composition of the blocks and mortar. It is also important to emphasize the influence of the water content within the built specimens. This water content was still in a process of draying on the occasions when the tests were carried out. This fact explains not only the differences between the values obtained in the laboratory tests and the values obtained by numerical simulation, but also the differences between the values obtained in the tests performed at different occasions. In addition, both the blocks and the mortar of the built specimens present small voids, coming from the manufacturing process, which of course are not present in the models used for the simulations. Despite simulated results are different from measurements, they show a consistent behavior, since simulations and measurements gets closer when the test structure loses its water content. Moreover, the measured and simulated currents increases and decreases in a similar way. This indicates that this method may be used to assess the internal properties of a masonry structure.

## 6. CONCLUSIONS

This paper explores the use of geo-electric tests in masonry specimens. Its primary purpose was to investigate how the size and shape of the electrodes interfere with electrical current and voltage values. The analysis was done using results from computational simulations by finite element method. Three-dimensional masonry models were used, taking into account all the geometrical characteristics of the specimens (blocks, joints, size and shape of the electrodes). Four small masonry specimens were designed and constructed to perform this task. Three types of electrodes were tested, and the electrode which produced the highest values and the largest current variations was the pin-type electrode, with insertion of 60 mm inside the mortar joints. Preliminary experimental tests were also conducted. The experimentally results were compared with the numerical simulations. There was a wide variation in the experimental results obtained in the two experimental tests, as well as in relation to the values obtained by numerical simulation. The differences can be explained by the high content of water in the specimens, no homogeneity of materials and unexpected anomalies within the specimens. In relation to the voltage, the size and shape of the electrodes slightly influence the measured values.

## ACKNOWLEDGEMENTS

The authors would like to acknowledge the Fundação para a Ciência e Tecnologia, which supported this research work as a part of the Project “Improved and innovative techniques for the diagnosis and monitoring of historical masonry”, PTDC/ECM/104045/2008.

The authors also would like to express their gratitude the São Paulo State University – Unesp – for having provided the necessary conditions for the development of this work.

## REFERENCES

[1] Daily W., Ramirez A., Binley A., LeBreque D. (2004) Electrical Resistance Tomography. In: *Leading Edge* 23: 438-442.

[2] Samouelian I., Cousin A., Tabbagh A., Bruand A., Richard G. (2005) Electrical Resistivity Survey in Soil Science – A Survey. *Soil & Tillage Research* 83: 173-193.

[3] Rucker D., Loke M., Levitt M., Noonan G. (2010) Electrical Resistivity Characterization of an Industrial Site Using Long Electrodes. *Geophysics* 93: 95-104.

[4] Zhou Q., Shimada J., Sato A. (2001) Three-Dimension Spatial and Temporal Monitoring of Soil Water Content Using Electrical Resistance Tomography. *Water Resources Research* 37: 273-285.

[5] Abu Zeid N., Balducci M., Bartocci F., Regni R., Santarato G. (2010) Indirect Estimation of Injected Mortar Volume in Historical Walls Using the Electrical Resistivity Tomography. *Journal of Cultural Heritage* 11: 220-227.

[6] Kruschwitz S., Niederleithinger E., Trela C., Wostmann J. (2012) Use of Complex Resistivity Tomography for Moisture Monitoring in a Flooded Masonry Specimen. *Journal of Infrastructure Systems* 18: 1-10.

[7] Keersmaekers R., Van Rickstal F., Van Gemert D. (2004) Geo-electrical Techniques as a Non-Destructive Appliance for Restoration Purposes. In *Proc. IV International Seminar on Structural Analysis of Historical Constructions*, Padua, 343-350.